Calcified Tissue International (2023) 112:525–542
https://doi.org/10.1007/s00223-022-01058-9

REVIEW ARTICLE

Contributions of Resin Cast Etching to Visualising the Osteocyte Lacuno-Canalicular Network Architecture in Bone Biology and Tissue Engineering

Mari Sato[1] · **Furqan A. Shah**[2]

Received: 5 October 2022 / Accepted: 21 December 2022 / Published online: 7 January 2023

Abstract

Recent years have witnessed an evolution of imaging technologies towards sophisticated approaches for visualising cells within their natural environment(s) and for investigating their interactions with other cells, with adjacent anatomical structures, and with implanted biomaterials. Resin cast etching (RCE) is an uncomplicated technique involving sequential acid etching and alkali digestion of resin embedded bone to observe the osteocyte lacuno-canalicular network using scanning electron microscopy. This review summarises the applicability of RCE to bone and the bone-implant interface. Quantitative parameters such as osteocyte size, osteocyte density, and number of canaliculi per osteocyte, and qualitative metrics including osteocyte shape, disturbances in the arrangement of osteocytes and canaliculi, and physical communication between osteocytes and implant surfaces can be investigated. Ageing, osteoporosis, long-term immobilisation, spinal cord injury, osteoarthritis, irradiation, and chronic kidney disease have been shown to impact osteocyte lacuno-canalicular network morphology. In addition to titanium, calcium phosphates, and bioactive glass, observation of direct connectivity between osteocytes and cobalt chromium provides new insights into the osseointegration potential of materials conventionally viewed as non-osseointegrating. Other applications include in vivo and in vitro testing of polymer-based tissue engineering scaffolds and tissue-engineered ossicles, validation of ectopic osteochondral defect models, ex vivo organ culture of whole bones, and observing the effects of gene dysfunction/deletion on the osteocyte lacuno-canalicular network. Without additional contrast staining, any resin embedded specimen (including clinical biopsies) can be used for RCE. The multitude of applications described here attest to the versatility of RCE for routine use within correlative analytical workflows, particularly in biomaterials science.

Keywords Bone · Osteocyte · Lacuno-canalicular network · Scanning electron microscopy · Resin cast etching

Osteocytes—the Master Orchestrators within Bone

The osteocyte lacuno-canalicular network (Ot.LCN) represents an important structural and functional component of bone [1], where the Ot.LCN architecture is closely related to bone material quality [2] and the mechanoresponsiveness of bone [3]. Not only do the osteocytes (Ot) represent > 95% of all the cells in bone [4], evidence from both in vitro and in vivo studies suggests that the osteocyte cytoskeleton, dendritic processes, integrin-based focal adhesions, connexin-based intercellular junctions, primary cilium, ion channels, and extracellular matrix are the major mechanosensors in osteocytes [5]. From each osteocyte, extensive numbers of cellular processes (also referred to as *dendritic projections* or *dendrites*) connect to the bone surface and the marrow space [6–9]. As many as ~ 42 billion osteocytes reside within the average adult human skeleton, and the total number of osteocyte dendritic projections is estimated to be ~ 3.7 trillion [10], which translates to about 88 dendrites per osteocyte. This lacuno-canalicular network (LCN) contains canalicular fluid, and facilitates the transport of various biomolecules

✉ Furqan A. Shah
furqan.ali.shah@biomaterials.gu.se

Mari Sato
satomari@den.hokudai.ac.jp

[1] Oral Biochemistry and Molecular Biology, Graduate School of Dental Medicine, Hokkaido University, Sapporo, Japan

[2] Department of Biomaterials, Sahlgrenska Academy, University of Gothenburg, Gothenburg, Sweden

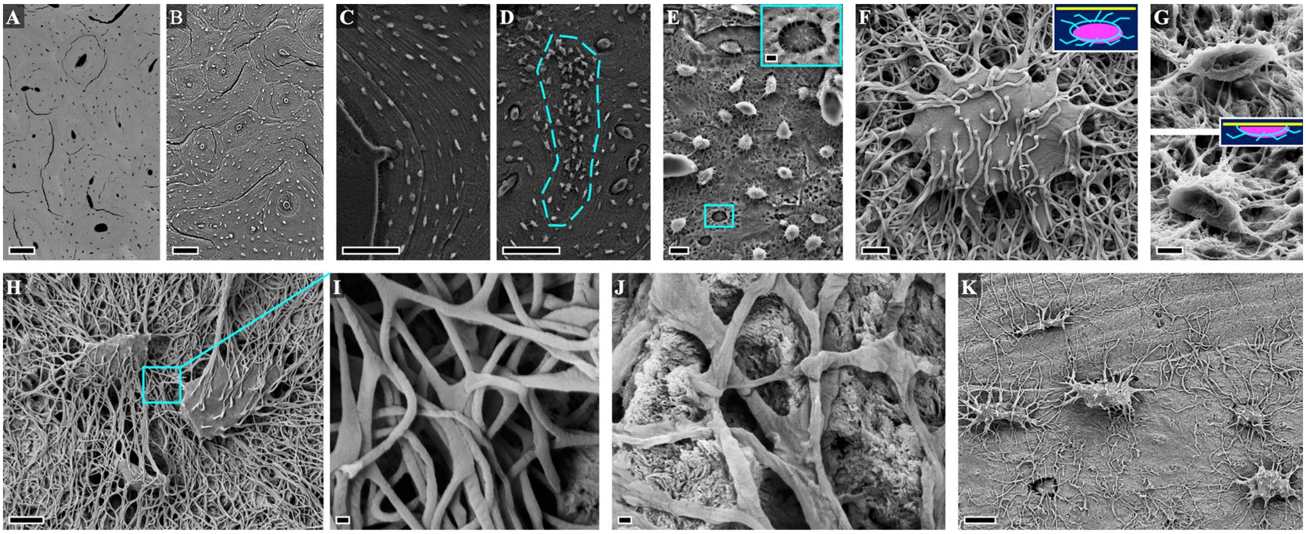

Fig. 1 Resin cast etching of bone. **A** Osteons in sheep cortical bone without resin cast etching (BSE-SEM). **B** Osteons in sheep cortical bone after resin cast etching. **C** Lamellar bone. **D** Woven bone (indicated by the broken line). **E** Osteocyte lacuno-canalicular network in rabbit cortical bone. Inset: An incompletely exposed osteocyte within a lacuna. Scale bar = 2 µm. **F** An osteocyte that was completely below the specimen surface before etching and therefore appears intact after etching. **G** Osteocytes that were already exposed at the specimen surface before etching and therefore appear partially cut after etching. Insets in F and G: Illustrations indicate osteocyte location in relation to the specimen surface (yellow line) prior to resin cast etching. **H**,**I** Osteocyte lacuno-canalicular network in rat bone. **J** Canalicular interconnectivity in human alveolar bone. **K** Osteocyte lacuno-canalicular network in human metacarpal bone. Scale bars in A, B, C, and D = 100 µm, E and K = 10 µm, F and G = 2 µm, H = 5 µm, I and J = 200 nm

(including small proteins) to and from the bloodstream [11], and is considered a key morphological component of osteocyte functionality where osteocytes communicate through gap junctions at the tips of the dendrites [12]. As mechanosensory cells, the osteocytes can sense shear forces caused by fluid flow through the pericellular space [13]. In order to maintain the connectivity of the Ot.LCN across the reversal front, during the remodelling process, the osteocytes can connect their existing dendrites with those of newly embedded osteocytes [6]. Anatomical evidence that the dendrites are in direct contact with the vasculature lends support to the notion that, independently of bone mass, the vascularity of the skeleton and thereby the Ot.LCN fluid volume are key determinants of bone strength [14]. Where the osteocytes play an important role in fracture healing [15], the precise architecture of the Ot.LCN varies with age, disease, and bone type (e.g., cortical or trabecular bone) [16]. Architectural and functional adaptations of the Ot.LCN are also witnessed around implanted biomaterials [17].

Resin Cast Etching and Scanning Electron Microscopy for Direct Visualisation of the Osteocyte Lacuno-Canalicular Network in Resin Embedded Bone

The Ot.LCN can be imaged with a diverse range of imaging techniques [18]. Variously referred to as *acid-etched resin cast(ing)* or simply *acid-etching*, resin cast etching (RCE) is a sample preparation technique to uncover the Ot.LCN within a limited depth/volume at the surface of a resin embedded specimen for direct visualisation using scanning electron microscopy (SEM) (Fig. 1) [19, 20]. By means of RCE, Curtis and co-workers (in 1985) reported a continuous LCN between osteocytes (described as '*flattened oval discs aligned parallel to the lamellae*') and the vasculature, extending the applicability of this technique to mineralised tissues other than dentine [21]. Preparation typically encompasses rendering the specimen flat by polishing (or alternatively using a thin section of undemineralised bone). The specimen is sequentially exposed to a mild acid, e.g., orthophosphoric acid (H_3PO_4) to remove the inorganic phase followed by digestion of the organic phase with sodium hypochlorite (NaOCl). Nevertheless, early investigators have also used hydrochloric acid (HCl) [22] rather than H_3PO_4.

The precise protocol requires optimisation due to interspecies differences in bone material properties. As the critical first step, however, the use of lower concentration acid (9% H_3PO_4) for a longer exposure time (~ 20–30 s) provides better control than application of higher concentration acid (37% H_3PO_4) for a shorter exposure time (~ 3–4 s) [19, 23]. In the second step, 5-min exposure to ~ 5% NaOCl affords an acceptable outcome. The specimen is gently rinsed in deionised water after each step, and finally allowed to dry at ambient conditions for several hours. Depending on the eventual imaging conditions, an electrically conductive coating (e.g., carbon, gold, gold–palladium, platinum, silver, etc.) may be necessary for SEM imaging. The quality of information obtained from the resin cast eventually depends on sample preparation. While a minor role is played by shrinkage artefacts related to fixation and dehydration [24], poor infiltration and polymerisation of the embedding resin may lead to artefacts such as areas that appear partially or completely devoid of Ot.LCN. This scenario can be particularly troublesome in the case of specimens that are too large or inhomogeneously dense to allow unimpeded flow of the embedding medium.

Using RCE, Okada and co-workers demonstrate variations in arrangement of the Ot.LCN between alveolar and basal areas of rat mandibles [25]. Progressing beyond qualitative descriptions of osteocyte shape, canalicular density, and overall vastness of the LCN, Pazzaglia and Congiu classified canaliculi into equatorial and radial types and established elegant quantitative metrics of Ot.LCN morphology, including osteocyte (or lacunar) density per unit surface area (#/mm^2), lacunar surface area (μm^2), number of canaliculi per osteocyte lacuna or dendricity (#/Ot.Lc), inter-lacunar canalicular length (μm), and canalicular diameter (nm) [26]. The osteocyte density is typically taken as the number of osteocytes or osteocyte lacunae per unit area of the mineralised compartment (N.Ot/B.Ar), but infrequently also taken as per total area, i.e., taking into consideration both the mineralised and unmineralised tissue compartments (N.Ot/Tt.Ar) [27]. Certain osteonal bone-specific metrics have also been defined. These include: (*i*) indirect canalicular connectivity, i.e., presence of connections between the radial canaliculi of an osteocyte and the transverse canaliculi of another osteocyte from a different lamella of the same osteon (%) [28], and (*ii*) intra-osteon maximum canalicular length, i.e., the longest visible canaliculus reaching the outermost lamella or a peripheral lacuna of the specific osteon (μm) [28, 29]. The information obtained by RCE can be further enriched by correlative backscattered electron scanning electron microscopy (BSE-SEM) [28, 30].

Compared to BSE-SEM, where only the osteocytes at the specimen surface can be seen, 2D imaging of the same field of view following RCE will reveal osteocytes in greater numbers, i.e., higher osteocyte density. The etching depth can vary as a function of reagent concentration and application time. With respect to the surface of a polished specimen (i.e., before RCE), the physical appearance of osteocytes located at the surface differs considerably from those present a few micrometres below the surface. Osteocytes at the specimen surface (seen by BSE-SEM) are partially cut and have lost some portion of the cell. On the contrary, sub-surface osteocytes (not seen by BSE-SEM) appear intact after RCE, since the entire cell becomes exposed, and are ideal candidates for quantitative measurements (e.g., dendricity).

Changes in Osteocytes Due to Ageing and Disease

The architecture of the Ot.LCN is altered in several conditions including ageing, osteoporosis, skeletal unloading, spinal cord injury, osteoarthritis, irradiation, and high calcium demand, and many of these changes have been investigated using RCE (Table 1).

Ageing

Okada and co-workers have reported distinct differences in Ot.LCN morphology between juvenile (3-week-old), adult (12-week-old), and aged (80-week-old) rats [25]. In juvenile rats, the osteocytes appear round while the canaliculi are short and thick. In adult rats, the osteocytes are ellipsoidal, with greater canalicular interconnectivity, as the canaliculi branch, twist, and fuse with neighbouring canaliculi to form an intricate network. Notably, the number of canaliculi going from an osteocyte to the central vascular canal is greater than the number of canaliculi going outward from the same lacuna to other neighbouring osteocytes. In aged rats, the osteocytes are slender and flat, with fewer canalicular communications, and a comparatively simpler canalicular network. In marine species such as the European eel (*Anguilla anguilla*), the osteocyte density declines from ~ 288 ± 110 mm^{-2} at the yellow (juvenile) eel stage, which lasts for 5–20 years, to ~ 201 ± 50 mm^{-2} at the silver (adult) eel stage. Artificial maturation can be accomplished through administration of human chorionic gonadotropin to male eels while carp pituitary extract and 17,20β-dihydroxy-4-pregnen-3-one to female eels. Such pharmacologically induced ageing results in the osteocyte density decreasing to ~ 134 ± 46 mm^{-2} prior to spawning towards the end of the silver eel stage [31].

Age-dependent variation in Ot.LCN interconnectivity is also reported in the human femoral cortex. In a cohort of young (20–40 y) and aged (70–95 y) individuals, the incidence of indirect canalicular connectivity is ~ 25% lower and the maximum canalicular length is 27% reduced in aged individuals. Furthermore, dendricity decreases

Table 1 Effect(s) of ageing and disease on the osteocyte lacuno-canalicular network

Condition	Species	Effect(s) on Ot.LCN	Refs
Ageing	Rat	Age-dependent change in osteocyte shape (from round to ellipsoidal and eventually flat) and decrease in canalicular interconnectivity/complexity	[25]
Natural and artificial ageing	European eel	Decreased osteocyte density in both natural and pharmacologically induced ageing	[31]
Ageing	Human	Age-dependent decreases in dendricity, indirect canalicular connectivity, and maximum canalicular length	[28]
Ageing	Human	Age-dependent decreases in dendricity and maximum canalicular length	[29]
Ageing	Human	Age-dependent decrease in dendricity	[32]
Osteoporosis	Rat (±OVX)	Decreased osteocyte density and dendricity due to OVX. Changes are reversed by Scl-Ab	[33]
Osteoporosis	Rat (±OVX)	No effect of hPTH, ALN, or RLX demonstrated	[35]
Osteoporosis	Rat (±OVX)	Regular osteocyte shape, higher dendricity, and branched canaliculi under stimulation with low-magnitude high-frequency vibration during fracture healing	[36]
Postmenopausal osteoporosis	Human	No change in Ot.LCN morphology in osteoporotic vs. age-matched healthy individuals	[29]
Skeletal unloading	Human	Greater loss of dendricity in long-term immobilised vs. age-matched osteoporotic and healthy individuals	[29]
Hindlimb suspension	Rat (±OVX)	Decreased osteocyte density and dendricity in normal/healthy and OVX animals. Changes are reversed by Scl-Ab	[33]
Spinal cord transection	Rat	Lower dendricity and osteocyte density per total area, deformed and disorganised osteocytes. Changes are reversed by Scl-Ab	[27]
Spinal cord transection	Rat	Lower dendricity. Changes are reversed by 15 Hz pulsed electromagnetic fields	[38]
Osteocytic osteolysis	Mouse (Ctsk-Cre/R26R)	Reversibly increased osteocyte lacunar area and canalicular diameter during high calcium demand	[39, 40]
Osteoarthritis	Human	Deformed, irregular-shaped osteocytes with fewer canaliculi	[41]
Irradiation	Dog	Decreased osteocyte density, dendricity, and canalicular connectivity between osteocytes and periosteum. Wider Haversian canals	[42]
Irradiation and implant healing	Dog	Narrower Haversian canals	[43]

by ~ 28%, from ~ 22 in young individuals to ~ 16 in aged individuals [28]. Similar trends have been reported in a cohort of young (34 ± 7 y) and aged (81 ± 7 y) individuals where dendricity decreases by ~ 12.4%, from ~ 19.4 in young individuals to ~ 17 in aged individuals, while the maximum canalicular length is ~ 37% reduced, from ~ 72 µm in young individuals to ~ 46 µm in aged individuals [29]. Similar age-related patterns in dendricity have also been reported in human auditory ossicles [32].

Osteoporosis, Skeletal Unloading, and Spinal Cord Injury

Morphological abnormalities of the Ot.LCN such as decreased osteocyte density and reduced dendricity are observed under experimentally induced osteoporosis via ovariectomy (OVX) in rats. These alterations are reversed by the administration of sclerostin monoclonal antibody (Scl-Ab) [33] and blockade of the protein sclerostin, which is an osteocyte-secreted Wnt signalling antagonist and inhibitor of bone formation [34]. Changes in local nanomechanical properties arising from different sequential treatment regimens of various anti-osteoporotic agents, e.g., human parathyroid hormone (hPTH), alendronate (ALN), raloxifene (RLX), have been correlated with osteocyte shape descriptors (i.e., major and minor axes) and osteocyte density in healthy and OVX rats. However, none of the therapeutic regimens led to demonstrable effects on the extracellular matrix nor did Ot.LCN morphology vary independently of extracellular matrix nanomechanical properties in OVX rats [35]. Stimulation with low-magnitude high-frequency vibration is associated with more regular osteocyte shape, increased dendricity, and densely branched canaliculi in both healthy and OVX rats from approximately one week through to six weeks post-fracture [36].

Related to increased sclerostin production by osteocytes due to skeletal unloading (i.e., disuse osteoporosis) [37], long-term immobilisation causes a specific pattern of cortical bone and osteocyte deterioration different from postmenopausal osteoporosis. In human femoral cortices of long-term immobilised, age-matched osteoporotic, and age-matched healthy females, dendricity in long-term immobilised individuals (~12) is lower than in aged-matched osteoporotic (~15) and age-matched healthy (~17) individuals. The intra-osteon maximum canalicular length is comparable between long-term immobilised (~48.9 µm), aged-matched osteoporotic (~ 52.7 µm), and age-matched healthy (~ 45.6 µm) individuals [29]. Interestingly, no differences in dendricity or maximum canalicular length are observed between postmenopausal osteoporosis and age-matched healthy females [29]. Hindlimb suspension has been used experimentally to simulate long-term immobilisation and disuse osteopenia in rodents. This condition has detrimental effects on osteocyte density and dendricity in both healthy and OVX rats. However, administration of Scl-Ab helps to restore the discrepancy [33].

Spinal cord injury is associated with abnormal neurological function and extreme immobilisation. Insights have been gained into the potential impact of traumatic spinal cord injury induced experimentally by transection of the spinal cord. In rats, the effects of spinal cord injury on the Ot.LCN are evident within 8 weeks [27, 38]. Administration of Scl-Ab once per week [27] and whole-body stimulation with pulsed electromagnetic fields [38] have been shown to be effective in restoring some of the alterations in Ot.LCN morphology following transection of the spinal cord. Transection at the 4th thoracic vertebra leads to ~30% lower dendricity and ~40% decreased osteocyte density per total area (i.e., including the marrow space), compared to spinal cord-intact animals. Systemic administration of Scl-Ab appears to counteract such alterations. Osteocyte density per bone area (i.e., excluding the marrow space), however, remains unaffected after spinal cord injury, with or without Scl-Ab. One explanation for this discrepancy between osteocyte density *per total area* and osteocyte density *per bone area* is loss of bone mass following spinal cord injury, which is in agreement with decreased bone volume (BV/TV) and increased trabecular spacing (Tb.Sp), as reported. Furthermore, the osteocytes in spinal cord-transected animals are markedly deformed, appearing round with a rough inner lacunar wall, and disorganised, while Scl-Ab treatment maintains the typical spindle shape and the well-ordered arrangement [27]. In a similar model, transection at the 12th thoracic vertebra leads to ~41% lower dendricity and consequently impaired dendrite connectivity compared to spinal cord-intact animals. However, 2 h per day exposure to pulsed electromagnetic fields delivered as a pulsed burst at 15 Hz frequency restores the deterioration in dendricity in spinal cord-transected animals [38].

Osteocytic Osteolysis, Osteoarthritis, and Irradiation

Cathepsin K (Ctsk) is a cysteine proteinase that mediates bone resorption and expressed not only in osteoclasts but also in osteocytes. In Ctsk-Cre/R26R mice, the osteocyte lacunar area increases reversibly in both cortical and trabecular bone during phases of high calcium demand, such as lactation, while a pronounced increase in canalicular diameter is observed only in trabecular bone [39, 40]. Degenerative conditions such as osteoarthritis are also associated with markedly deformed osteocytes having an irregular and rounded appearance and very few canaliculi compared to spindle shaped, well-organised and interconnected osteocytes in bone from individuals without subchondral bone sclerosis or cartilage degeneration [41]. Irradiation also leads to changes in Ot.LCN morphology and the vasculature. In the alveolar bone, the most dramatic change is seen in dendricity, from ~17 in nonirradiated bone to ~9 in irradiated bone, i.e., a ~44% reduction. Likewise, canalicular connectivity between osteocytes and the periosteum is also impaired. And while osteonal diameter is not affected, the Haversian canals in irradiated bone are ~28% wider and osteocyte density is reduced by ~12%. [42]. Irradiation compromises the healing environment for osseointegrated implants. In previously irradiated alveolar bone, the peri-implant Ot.LCN and vasculature have been shown to be particularly affected. However, following submerged healing of commercially pure titanium (cp-Ti) cylinders to restore masticatory function, the Haversian canals in irradiated bone are found to be ~22% narrower [43]. This reduction in Haversian canal diameter is contrary to observations in native bone [42], suggesting differences between how irradiation impacts native bone and how the healing environment might respond post-irradiation.

The Osteocyte Lacuno-Canalicular Network in Transgenic Animal Models

In several animal models of gene dysfunction, altered osteocyte morphology and organisation of the associated canalicular network have been demonstrated using RCE (Table 2).

Dentine Matrix Protein-1, Klotho, and Dentine Sialophosphoprotein

In the absence of dentine matrix protein-1 (DMP-1), e.g., *Dmp1* null mice, the inner lacuno-canalicular wall appears rough and buckled, and fewer canaliculi are present [44, 45]. Furthermore, abnormal lacuno-canalicular system in *Dmp1* knockout bone shows a reduction in the number of canaliculi but enlarged osteocyte lacunae with rough lacunar walls. Re-expression of full-length DMP-1 rescues the skeletal abnormalities of *Dmp1* null mice [46]. There is also evidence of periodontal breakdown in the *Dmp1* null mouse model of hypophosphatemic rickets, where the Ot.LCN is disorganised, lacunae are clustered together, and a large amount of osteoid is present [47]. Expression of dentine

Table 2 Summary of RCE findings from investigations of gene dysfunction

Gene or PROTEIN	Ot density	Canaliculi	Ot Distribution	Ot Size	Ot Shape	LCN	Osteoid	Ot.LCN walls	Refs
DMP-1[†]	–	Decreased ↓	Clustered; Disorganised	Larger ↑	Deformed	–	More ↑	Rough; Buckled	[44–49]
Klotho	–	Decreased ↓	Randomly oriented	–	–	–	–	–	[50]
DMP-1 and Klotho	–	Decreased ↓	Disorganised	Larger ↑	–	–	–	–	[50]
DSPP	–	Decreased ↓	Irregular	Larger ↑	–	Disorganised; Reduced propagation	–	–	[51]
DSPP N-terminus overexpression	–	Decreased ↓	Irregular	–	Deformed	Disorganised	–	–	[52]
Col4a3[††]	–	–	–	–	Round	–	–	–	[53]
Osx	Low ↓	Decreased ↓	–	–	Deformed	–	–	–	[54]
BMPR-1A	High ↑	Decreased ↓	Irregular; Disorganised	Larger ↑	–	–	–	–	[55]
ERK-1, ERK-2	–	Decreased ↓	–	–	–	–	–	–	[56]
Nf1	–	Decreased ↓	Irregular; Disorganised	–	Deformed, Round	Disorganised	–	Coarse	[57, 58]
CSF-1	Low ↓	Decreased ↓	Disorganised	–			More ↑	Rough	[60]
FAM20C	–	Decreased ↓	–	–	Abnormal, Deformed		–	–	[62, 63]
Phex	–	–	–	–		Severely disturbed	More ↑	Buckled	[64]
Vhl	Low ↓	Decreased ↓	Disorganised; Randomly oriented	–	Deformed		–	–	[65]

[†] Transgenic expression of DSPP rescues Ot.LCN defects observed in *Dmp1* knockout mice [48, 49]

[††] Genetic or pharmacological supplementation with DMP1 corrects osteocyte morphological changes [53]

sialophosphoprotein (DSPP*)* is markedly reduced in *Dmp1* knockout mice, where the osteocyte lacunae appear larger, and disorganised with fewer canaliculi, both in alveolar bone and in long bones [48, 49]. Transgenic expression of DSPP rescues Ot.LCN defects noted in *Dmp1* knockout mice to varying levels in the alveolar bone [48] and in the femur [49]. Furthermore, in *Dmp1* and Klotho deficient ($Dmp1^{-/-}$ *kl/kl*) mice, osteocytes are poorly organised, visibly larger in size, and exhibit a complete lack of dendritic processes. In Klotho-deficiency, alone, only a moderate reduction in the number of canaliculi and random orientation of osteocytes are observed [50]. In *Dspp* null mice, osteocyte lacunae appear larger and irregularly distributed, along with disorganised and fewer canaliculi that exhibit a markedly reduced propagation into the surrounding bone [51]. Overexpression of the NH$_2$-terminal fragment of DSPP further aggravates the periodontal defects of *Dspp* null mice. The spectrum of morphological alterations is similar to *Dspp* null mice, but more intense, where the osteocyte lacunae in the alveolar bone appear irregular with disorganised and fewer canaliculi [52].

Collagen Alpha-3(IV) Chain

The 129SvJ $Col4a3^{-/-}$ and B6 $Col4a3^{-/-}$ mouse models lack the collagen alpha-3(IV) chain (Col4a3) and display several features of human chronic kidney disease, including progressive loss of kidney function and alterations in bone and mineral metabolism. Compared to their respective wild-type counterparts, *Col4a3* null mice exhibit round osteocytes. However, genetic or pharmacological supplementation with DMP-1, which plays a key role in terminal differentiation of osteocytes, has been found to correct the morphological alterations in *Col4a3* null mice [53].

Osterix

The osteoblast-specific transcription factor osterix (Osx) is required for osteoblast differentiation into mature osteoblasts and osteocytes. Postnatal ablation of Osx leads to markedly deformed osteocytes, a decreased number of osteocytes throughout the cortex (close to both periosteum and endosteum, and in the middle of the cortex), and very few canaliculi resulting in a greatly reduced density of the canalicular network [54].

Bone Morphogenetic Protein Receptor Type 1A

Bone morphogenetic proteins (BMPs) are multi-functional growth factors and are known to regulate bone development and regeneration. Bone morphogenetic protein receptor type 1A (BMPR-1A) is a potent receptor of BMP. Defective osteocyte formation and morphology are observed in conditional knockout mice with deletion of *Bmpr1a*. The osteocytes appear enlarged with a sharp increase in osteocyte density and a poor spatial distribution pattern, and severe reduction in the number of canaliculi [55].

Extracellular Signal-Regulated Kinase

The extracellular signal-regulated kinase (ERK) mitogen-activated protein kinase (MAPK) pathway plays an essential role in mediating fibroblast growth factor signalling in skeletal cells. In the absence of ERK-1 and ERK-2 in limb mesenchyme of *Prx1-Cre* mice, the osteocytes lack dendritic processes, indicating that ERK-1 and ERK-2 inactivation disrupts the formation of the Ot.LCN [56].

Neurofibromin 1

Neurofibromin is an important protein for skeletal development and growth. Inactivation of *Nf1* in the mesenchymal lineage of *Nf1Prx1* mice results in severe skeletal pathology in osteoblast-specific conditional knockout mice. In *Nf1Prx1* mice, the osteocytes are irregularly distributed, less elliptical (or more spherical) and their orientation deviates from the expected lamellar direction, and the canalicular network is disorganised. Furthermore, the morphological changes are most pronounced in the proximity of muscle attachment sites, which are areas exposed to high mechanical loads [57]. *Nf1* deletion has also been shown to result in a disorganised distribution of osteocytes in osteocyte-specific conditional knockout mice. Moreover, the canaliculi are disorganised and coarse, and the number of canaliculi per cell is significantly reduced. Overall, *Nf1* deficiency in osteocytes appears to disrupt the mineralisation process, leading to an osteopenic change and osteomalacia-like bone phenotype [58].

Colony-Stimulating Factor 1

Colony-stimulating factor 1 (CSF-1) is highly expressed by osteoblasts and osteocytes to regulate osteoclast-mediated bone remodelling [59]. Disruption of CSF-1 leads to osteopetrosis and osteocyte defects. RCE shows that *Csf1* knockout osteocyte lacunae are disorganised, decreased in number, and have rough walls. In addition to significant reduction in the overall density of the dendrite network, large amounts of osteoid are present in the extracellular matrix [60].

Golgi Serine/Threonine Protein Kinase FAM20C

Human FAM20C and mouse DMP4 amino acid sequences are 69% identical (73% similar) [61]. Using conditional knockout mice with mineralised tissue-specific deletion of *Fam20c*, FAM20C has been shown to play a critical role in the development of the vertebra [62, 63]. Here, osteocytes in the vertebrae [62] and tibiae [63] of conditional knockout mice appear to lose their normal morphology and have fewer canaliculi.

Phosphate-Regulating Neutral Endopeptidase

In global and conditional (osteoblasts and osteocytes) phosphate-regulating neural endopeptidase (*Phex)* knockout mice, the inner lacuno-canalicular wall appears buckled and enlarged, with severely disturbed canalicular organisation in addition to abundant osteoid. Aberrant PHEX function, therefore, leads to a bone phenotype indistinguishable from that of hypophosphatemic (*Hyp)* mice, the murine homolog of human X-linked hypophosphatemia and Vitamin D resistant rickets [64].

Von Hippel-Lindau Tumour Suppressor

The E3 ubiquitin ligase von Hippel-Lindau targets various proteins for degradation, including hypoxia-inducible factor 1-alpha (HIF-1a), and is expressed in many tissues and cell types. Disruption of the von Hippel-Lindau (*Vhl)* gene in mature osteoblasts/osteocytes in mice activates the HIF-1 signalling pathway in osteocytes, which results in disorganised, randomly oriented, and irregularly contoured osteocytes. The osteocyte density is decreased together with the presence of fewer canaliculi [65].

Osteocytes in Peri-Implant Bone

The osteocytes and the associated LCN are fundamental components of bone formed around implant biomaterials [66]. These include load-bearing implants intended for permanent anchorage in bone (typically metals and alloys), degradable biomaterials that stimulate new bone formation and gradually resorb, and tissue engineering scaffolds seeded with various relevant cell types and biological cues (Fig. 2).

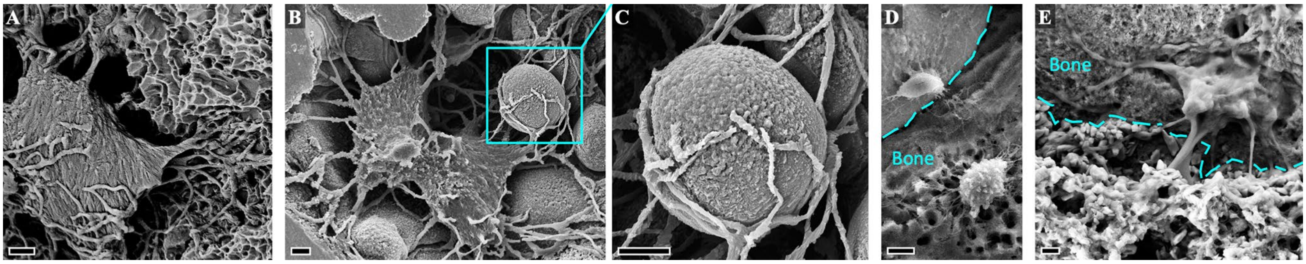

Fig. 2 Osteocytes in peri-implant bone. **A** Osteocyte attachment via interdigitation between canaliculi and the topographical features of an acid-etched titanium implant in rat bone. **B**,**C** Canaliculi wrapped around a spherical feature on a selectively laser-ablated titanium implant in rabbit bone. Adapted with permission from Shah et al. 2019. Copyright 2019, Elsevier [66]. **D** Direct connectivity between osteocytes and a 3D printed CoCr implant in rabbit bone (broken line demarcates the bone-implant interface). **E** An osteocyte attached to a multi-component CaP implant in sheep bone (broken line demarcates the bone-implant interface). Scale bars in A, B, and C = 2 µm, D = 5 µm, E = 1 µm

Osseointegrated Metallic Biomaterials

The Ot.LCN in peri-implant bone shows several structural changes related to factors such as healing kinetics and the physico-chemical properties of the implant biomaterial [17]. Presumably, a dense and well-aligned network of dendritic processes in the vicinity of the implant surface may be able to detect compressive and tensile strains imposed on the interfacial tissue, allowing for structural adaptations to maintain homeostasis. Speculatively, close adaptation and attachment of the lacuno-canalicular network to the implant surface may behave as a physical factor contributing towards bone-implant interlocking. Direct attachment of osteocytes to the surface of implants, through dendritic processes, is worth examining [67, 68], and in principle, can be observed as early as mineralised bone is detectable after implantation. When witnessed between osteocytes and materials otherwise considered to integrate poorly, e.g., CoCr [69, 70], such direct connectivity is interpreted as evidence of osseointegration.

RCE has been employed extensively to observe the spatial relationships between the Ot.LCN and bone anchored implants, including topologically modified titanium [71, 72]. Osteocytes are generally aligned with their long axes parallel to the implant surface with long canaliculi extending towards it. Osteocytes form an interconnected lacuno-canalicular system and attach, through canaliculi, to acid-etched [71] and grit-blasted [72] surfaces. Interconnectivity between neighbouring osteocytes and formation of extensive canalicular networks in the vicinity of the implant surface implies cell-to-cell communication. Where implant surface features are of appropriate dimensions, e.g., sub-micron topography achieved through acid-etching, the canaliculi can closely interdigitate with the topographical features [71]. Direct attachment of osteocytes to alumina grit-blasted implants has also been demonstrated in OVX rats [73]. Furthermore, highly interconnected osteocytes are also reported adjacent to nanopatterned implant surfaces characterised by ~ 75 nm wide hemispherical features produced by colloidal lithography [30]. Nanopatterning achieved by alkaline-etching also has a demonstrable positive impact on osteocyte dendricity compared to acid-etched, micro-rough implants in a rat model [74].

Laser-ablation of titanium under ambient conditions generates a 50–200 nm thick surface TiO_2 layer that is superimposed over micrometre-sized droplets of resolidified metal. Experiments conducted in rabbits show that canaliculi extend several micrometres towards the implant surface [67]. Interestingly, the canaliculi remain attached to the implant surface despite the application of disruptive mechanical forces such as during the acquisition of removal torque measurements. Adjacent to functionally loaded laser-ablated clinical dental implants (i.e., in human), osteocytes are aligned parallel to both the lamellar direction of bone and to the micrometre-scale contour of the implant surface, which points towards an important role of implant surface contour in guiding the eventual microstructure of peri-implant bone. From these osteocytes, canaliculi not only extend towards the implant surface and branch in close proximity to the channel-like surface TiO_2 layer but also extend in the opposite direction (i.e., away from the implant surface) towards Haversian canals [75].

In newly formed bone adjacent to micro-rough implants [72] and additively manufactured macro-porous Ti6Al4V implants [68], the osteocyte density is typically higher than in the native bone distant from the implant. Higher osteocyte densities are attributable to the presence of relatively younger bone (compared to native bone) and woven bone that is yet to remodel. Tantalum coatings on porous additively manufactured Ti6Al4V fracture-fixation plates also support the attachment of osteocytes through interconnected canaliculi, providing further evidence in favour of the osseointegrative properties of tantalum [76].

At least in small animal models, repetitive mechanical loading of osseointegrated implants has been shown to increase osteocyte density together with changes in osteocyte morphology such as decreased ellipticity and higher dendricity in peri-implant bone [77]. In experimental setups without mechanical stimulation/loading, a disorganised arrangement of osteocytes is noted in areas of new bone adjacent to micro-rough implants compared to areas of native lamellar bone [72]. Similar observations have been made in OVX rats, where adjacent to both minimally rough and micro-rough implant surfaces, the osteocytes exhibit a disorganised arrangement and appear less elliptical than those in native lamellar bone [73].

Osteocyte attachment to highly complex, additively manufactured, macro-porous geometries has also been reported [68, 69]. After long-term submerged healing in sheep, the dendricity adjacent to the surface of additively manufactured, macro-porous and solid Ti6Al4V implants is 38–42% higher than in areas of native lamellar bone [68]. Here also, osteocytes adjacent to the implant surface appear less elliptical, but somewhat larger than those in areas of native lamellar bone [68].

In bone adjacent to functionally loaded, laser-ablated clinical dental implants, the dendricity in peri-implant bone (~ 25) is higher than in the native bone outside the implant thread (~ 17), pointing towards biomechanical differences between the two anatomical locations [75].

Degradable Biomaterials for Bone Repair

Certain bone repair materials are designed to degrade in vivo. Consequently, the bone-biomaterial interface migrates over time. It has been demonstrated that bioactive glass supports osteocyte attachment via dendritic processes that appear to pass through the calcium phosphate (CaP) rich interfacial layer and reach the silica rich surface of the reacted bioactive glass [78]. A concentric arrangement of the Ot.LCN in bone that is formed in response to multi-component CaP materials, beyond the physical confines of the skeletal envelope, offers evidence for remodelling in extraskeletal bone [79]. Composite beads containing a pullulan–dextran mixture as the organic phase and hydroxy(l) apatite as the inorganic constituent have been investigated in a sinus floor augmentation model in sheep. The presence of a dense network of osteocytes has been reported around the organic–inorganic composite beads with numerous zones of cells in direct contact with the microbeads, at 3 and 6 months, with evidence of neovascularisation and direct contact between osteocytes and blood vessels [80]. Similar observations have been made for clinically used deproteinised bovine bone mineral (Bio-Oss®) in a sinus floor augmentation model in sheep. The bone formed around deproteinised bovine bone mineral particles is characterised by highly aligned networks of osteocytes, and connectivity between osteocytes and neighbouring blood vessels through canaliculi [80].

Tissue Engineering Scaffolds and Tissue-Engineered Ossicles

3D printed polycaprolactone (PCL) scaffolds with CaP coatings and recombinant human bone morphogenetic protein 7 (rhBMP-7) has been a popular direction in bone tissue engineering. When PCL-CaP constructs seeded with either human mesenchymal stem cells or human primary osteoblasts are loaded with rhBMP-7 and subcutaneously implanted in immunodeficient mice, an abundance of morphologically intact osteocytes with highly interconnected dendritic processes is witnessed by 8 weeks post-implantation. As may be expected, the osteoblasts lead to ~ 79% more osteocytes per unit area than the human primary mesenchymal stem cells [81]. Segmental tibial defects in sheep treated with PCL-CaP constructs loaded with both platelet-rich plasma and rhBMP-7 show mainly woven bone with a disorganised arrangement of osteocytes by three months post-implantation. The canalicular network appears mostly disrupted and damaged. The woven bone is widely replaced by lamellar bone at 12–15 months post-implantation. In addition to the presence of blood vessels and primary osteon formation, osteocytes are found in direct contact with scaffold struts [82]. Human mesenchymal stem cells can also be seeded onto tubular PCL-CaP constructs by sequential static culture followed by dynamic culture in a rotating bioreactor. Loaded with rhBMP-7 and embedded in fibrin glue, such constructs are subcutaneously implanted in immunodeficient mice to obtain tissue-engineered, humanised ossicles. At 10–14 weeks, an abundance of osteocytes with highly interconnected dendritic processes has been interpreted as a functional osteocyte network within the newly formed bone [83, 84].

Medication-Related Osteonecrosis of the Jaw and BMP-2 Delivery

RCE has been found to be useful in evaluating a model multi-component hydrogel system consisting of star-shaped polyethylene glycol, Arg-Gly-Asp tripeptides, and maleimide functionalised heparin as a delivery mechanism for rhBMP-2. In a rat model of medication-related osteonecrosis of the jaw (MRONJ), induced by zoledronic acid infusion after tooth extraction, controlled release of rhBMP-2 is associated with increased osteocyte density. On the other hand, defects not treated with rhBMP-2 show empty lacunae, attributable to areas of non-vital bone, which is consistent with the expected histological appearance of MRONJ where hematoxylin and eosin staining demonstrate karyorrhexis, karyolysis, and pyknosis [85].

Unconventional Applications of Resin Cast Etching

RCE has been employed in several unique scenarios. In mouse femurs maintained under ex vivo culture, exposure to transforming growth factor-beta 1 (TGF-β1) increases dendricity while TGF-β1 receptor inhibition reduces dendricity [86]. In tissue engineering using primary human osteoprogenitor cell-laden tubular PCL-CaP constructs, detection of osteocyte-like dendritic cells points towards in vitro osteogenic differentiation of the seeded cells [87]. Likewise, preservation of Ot.LCN architecture in bovine osteochondral plugs supplemented with rhBMP-7 and subcutaneously implanted in rats attests in favour of this setup as an ectopic osteochondral defect model [88]. It has also been demonstrated that osteocytes within autogenous bone fragments generated in situ during osteotomy procedures can reconnect with osteocytes in de novo bone found on the surface of such fragments, thereby restoring canalicular connectivity across the old–new bone interface [89]. In the lumbar vertebrae of toothed whale species *Physeter macrocephalus* and *Orcinus orca*, differences in Ot.LCN connectivity have been attributed to dissimilarities in metabolic activity and diving behaviour [90]. Furthermore, RCE has also found utility in detecting Ot.LCN in multimillion-year-old fossils (e.g., of a Late Cretaceous Mosasaur, Prognathodon) [91], examining the bacterial biofilm in MRONJ [92], and determining the extent of microdamage induced by self-tapping screw insertion in cadaver bone [93]. Finally, the combination of RCE and multibeam SEM has enabled the creation of seamlessly navigable anatomic maps of human bone and the relevant cellular components. The Google Maps JavaScript API navigational platform has been used to generate navigable maps of regions imaged using a 61-parallel-beam SEM (such as the Zeiss MultiSEM) [94]. Through a geographical information system approach, disease epidemiology can be conducted by network modelling, where spatial information is acquired by localising exposed landmarks such as osteocytes and blood vessels [95]. Introduction of machine learning to handle large datasets has further advanced the multibeam SEM approach. Knothe Tate et al. report a dataset comprising ~ 1810 mm^2 tissue (> 7 million images and ~ 11 terabytes of data) where ~ 206,180 osteocytes were detected and classified at > 92% accuracy within 100 h [96].

Advantages of Resin Cast Etching and Comparison with Other Techniques

Although access to an SEM is necessary, RCE is an uncomplicated approach to direct visualisation of the Ot.LCN, even if moderately destructive. Specimen geometry is not a significant limitation. Large fields of view can be imaged quickly and the precise imaging conditions can be adjusted to achieve either improved contrast of resin-filled structures (e.g., at high accelerating voltage) or for finer details (e.g., low accelerating voltage and short working distance). Since no specific processing procedures such as demineralisation or contrast staining are necessary, RCE does not interfere with correlative analytical workflows [97]. Any clinical material (e.g., human bone biopsies) can be used provided that the specimen is undecalcified and embedded in resin. Within the SEM, the specimen may be tilted to high angles (up to 70° in some instruments) to reveal features hidden behind overhanging structures. Finally, a nominally intact surface can be easily recovered by polishing away the etched volume. It is important to note that, with RCE, the osteocyte cell body or the dendrites are not directly observed. What is seen, in fact, is the resin that has infiltrated into the pericellular space, enclosing the dendrite and the cell body. The lateral dimensions of the resin cast, therefore, represent the bony walls of the LCN. Therefore, the surface of the resin cast essentially reflects the inner wall of the Ot.LCN as opposed to the outer surface of the cell body or the dendrite. Besides RCE, several other analytical techniques can be used to image the Ot.LCN (Table 3).

Scanning Electron Microscopy

Various protocols have been described for stepwise removal of the inorganic and organic components of bone for direct observation of the cellular components using SEM. The HCl–collagenase method described by Ejiri and Ozawa [98] is analogous to the approaches involving ethylenediaminetetraacetic acid (EDTA) followed by either potassium hydroxide (KOH) [99] or sodium hydroxide (NaOH) [100] approaches. Paraformaldehyde and/or glutaraldehyde fixed bone specimens are used. In the first step, bone mineral is removed with HCl or EDTA, followed by elimination of the organic matrix by exposure to collagenase, KOH, or NaOH, and post-fixation with osmium tetroxide (OsO_4). Although the bone specimen is not resin embedded, the 3D information obtained is remarkably similar to RCE. Two related SEM-based techniques generate 3D information through serial sectioning and 3D reconstruction, (*i*) focussed ion beam scanning electron microscopy (FIB-SEM) and (*ii*) serial block-face scanning electron microscopy (SBF-SEM).

Table 3 Other analytical techniques to image the osteocyte lacuno-canalicular network

Technique	Method	Advantage(s)	Disadvantage(s)
SEM	HCl–collagenase [98]		Dedicated specimen required
	EDTA–KOH [99]		Dedicated specimen required
	EDTA–NaOH [100]		Dedicated specimen required
	(P)FIB-SEM [101–103]	Serial sectioning and 3D reconstruction	Small volumes analysed; up to ~ 16,000 µm^3 using PFIB [103]
	SBF-SEM [104]	Serial sectioning and 3D reconstruction Demineralisation (and OsO4 staining) improves contrast of subcellular structures and is less damaging to the ultramicrotome knife	Small volumes analysed. Metal implant (if present) must be removed. Demineralisation reduces contrast between cells and the surrounding matrix
TEM	Ultramicrotomy [24, 105]	Measurement of lateral dimensions of canaliculi, dendrites, microfilaments. Imaging of 0.5–1 µm thick sections using HVEM [108–110]. Tomography of 1–3 µm thick sections using UHVEM [113, 114]	Demineralisation is typically required. Metal implant (if present) must be removed [106–110]
	FIB lift-out [75, 111, 112]	Site-specific sample preparation Nanoscale characterisation of intact bone-biomaterial interface	Very small areas analysed (~ 20 × ~ 8 µm^2)
CLSM	Fluorescent dyes [16, 36, 115–117]	Volumetric/depth imaging	Photobleaching
	Immunostaining [118–122]	Volumetric/depth imaging. Labelling of cytoskeleton, cell membrane, nucleus, gap junctions	Photobleaching
Multiphoton microscopy	3PEF [115, 125]	Intravital imaging of osteocytes [123]	Staining with fluorescent dyes Photobleaching
	THG [115, 125]	Label-free imaging of porosity (osteocytes, canaliculi, blood vessels)	Resin embedding reduces the contrast of canaliculi
Deconvolution microscopy	Fluorescent dyes [126]	Excellent lateral (x–y plane) resolution	Poor axial (z-direction) resolution. Need for fluorescent staining .
LSFM	Bone CLARITY [127]	3D fluorescence imaging up to 1.5 mm depth	Tissue clearing (including demineralisation and delipidation) required
SR-CT	X-rays [128–131]	High resolution and level of detail	Small volumes are sampled Limited access to SR facilities
AFM	EDTA [132] or HCl–NaOCl [133]	High resolution and level of detail Measurement of tissue mechanical properties	Surface preparation required to expose structures of interest Small areas are mapped

FIB-SEM reveals significantly higher level of detail than the various optical imaging techniques. With gallium (Ga^{3+}) as the liquid–metal ion source in most FIB instruments, serial sectioning is carried out for later 3D reconstruction. The main drawback of this approach is that extremely small volumes are typically analysed. Consequently, it is important to know beforehand where the osteocytes are located. Therefore, often, only those osteocytes are selected for imaging that are already exposed at the specimen surface (and therefore partially cut and incomplete) [101, 102]. This specific challenge is circumvented by recent advancements in plasma focussed ion beam (PFIB) technology, which enables large volume analysis (e.g., up to ~ 16,000 µm^3) [103].

SBF-SEM involves automated, sequential BSE-SEM and ultramicrotome sectioning of a sample within the SEM. Both demineralised (decalcified and stained with OsO_4) and undemineralised tissues can be used for SBF-SEM. The technique is, however, inherently destructive, the obtained images are non-isotropic, and the surface is rendered potentially unusable for correlative analytical platforms involving vibrational spectroscopy and crystallography [18, 104]. The advantages of decalcifying bone tissue for SBF-SEM include (*i*) greater ultrastructural image contrast, making automated segmentation of subcellular structures easier, (*ii*) improved image quality, and (*iii*) less damage to the diamond ultramicrotome knife. The disadvantages of decalcification are that (*i*) the tissue is further from the native state, (*ii*) the image contrast between the cells and surrounding matrix is reduced, making automatic segmentation of the lacunae more difficult, and (*iii*) the time required to prepare the decalcified sample is considerably longer than the mineralised sample [104].

Transmission Electron Microscopy and Electron Tomography

Transmission electron microscopy (TEM) allows extremely precise measurement of lateral dimensions (i.e., diameter) of canaliculi, osteocyte dendrites (cytoplasmic processes), and microfilaments [105]. Routine TEM, using < 100 nm thick sections, also reveals artefacts related to sample preparation, e.g., shrinkage at the cell–matrix interface [24]. In the specific case of bone-implant specimens, if the TEM section must be obtained by ultramicrotomy, the metal implant must first be removed by either mechanical separation under a dissection microscope [106, 107] or cryofracturing [108–110]. Undemineralised, ultramicrotomed sections ranging in thickness from ~ 250–500 nm [108, 109] to 1 µm [110] have been examined using high voltage electron microscopy (HVEM) at 1000 kV. Using a FIB instrument to *lift-out* an electron transparent specimen, selected osteocytes (including those adjacent to metal implants) can be milled out from undemineralised bone for *Z*- (atomic number) contrast, scanning transmission electron microscopy [111, 112] and electron tomography [75]. Other possibilities for electron tomography include ultra-high voltage electron microscopy (UHVEM) at 2000 kV, where a ± 60° tilt series is collected at 2° intervals, using 1 µm thick sections [113], or 3 µm thick sections stained with silver proteinate (protargol) solution [114].

Confocal Laser Scanning Microscopy

Several closely related methods using confocal laser scanning microscopy (CLSM) have been described for visualising the Ot.LCN. Ethanol fixed and dehydrated bone, stained with 0.1–1% fluorescein isothiocyanate (FITC) can be used for 2D [115] and 3D imaging [36, 116]. Similarly, formalin fixed and dehydrated bone can be stained with 1% Basic Fuchsin for determining lacunar volume, lacunar surface area, osteocyte density, and dendricity, however accurate measurement of volume and surface area of 3D structures requires an axial correction to overcome distortion in the *z*-direction [16]. Rhodamine-6G is another highly effective dye for imaging the LCN [117]. In avian/chicken bone, osteocytes can be selectively localised by incubation with the monoclonal antibody OB7.3, followed by fixation in 3% paraformaldehyde, permeabilisation with Triton-X, and incubation with an appropriate secondary antibody (e.g., Alexa Fluor® 488 conjugated chicken anti-mouse IgG antibody) [118]. Cell–cell communication across gap junctions between osteocytes can be observed by fluorescence recovery after photobleaching (FRAP) experiments [119, 120], where the gap junctions are localised by immunostaining for the protein connexin 43 [121]. More advanced *multiplexed* methods require demineralisation and immunostaining of the osteocyte cytoskeleton, cell membrane, nucleus, and the LCN, while the collagen can be visualised in transgenic mice expressing green fluorescent protein tagged collagen [122].

Multiphoton Microscopy

Multiphoton microscopy, e.g., two- and three-photon excitation, enables intravital imaging of biological tissues such as bone [123]. Two-photon excited fluorescence (2PEF) and second harmonic generation (SHG) and primarily highlight the extracellular matrix [115, 124], while three-photon excited fluorescence (3PEF) and third harmonic generation (THG) reveal the Ot.LCN [115, 125]. In contrast to 2PEF and 3PEF, SHG and THG allow label-free imaging of certain fibrillar/tubular structures and heterogeneities such as interfaces within tissues.

Deconvolution Microscopy

Deconvolution microscopy of formalin fixed and dehydrated bone, stained with 1% FITC also allows quantitative analysis of the LCN. A horizontal plane approximately 1 µm *above* the osteocyte cell body is imaged, which is expected to contain dendrites that fan out radially [126]. Despite excellent lateral resolution, radially extending dendrites cannot be assessed accurately owing to poor axial resolution.

Light-Sheet Fluorescence Microscopy with Tissue Clearing

The tissue clearing method “Bone CLARITY” (Clear Lipid-exchanged Acrylamide-hybridised Rigid Imaging/Immunostaining/In situ hybridisation–compatible Tissue hydrogel) combined with light-sheet fluorescence microscopy (LSFM) enables visualisation of osteoprogenitors within bone marrow in whole/intact bone. Clearing renders intact bones transparent, for an imaging depth of up to ~ 1.5 mm, while preserving endogeneous fluorescence. Currently, this approach has only been reported for specialised, transgenic animal models, where fixation in 4% paraformaldehyde was followed by demineralisation in 10% EDTA demineralisation and delipidation with sodium dodecyl sulphate [127].

Synchrotron Radiation X-ray Computed Tomography

Synchrotron radiation X-ray tomography (SR-CT) reveals the osteocytes and canalicular interconnectivity in exceptionally high detail. Although the scanned sub-volumes tend to be small [128–130], the obtained data on canalicular interconnectivity can be extended for simulation of LCN fluid flow dynamics [131].

Atomic Force Microscopy

Imaging the LCN using atomic force microscopy (AFM) requires some form of surface preparation. A one-step demineralisation using EDTA is sufficient for unembedded bone [132] while a two-step procedure involving the use of HCl and NaOCl is required for poly(methyl methacrylate) embedded bone [133].

Technical Challenges in Imaging Osteocytes Around Implant Biomaterials

Numerous challenges arise in the pursuit of visualising direct contact between implant biomaterials and the Ot.LCN within peri-implant bone. Techniques that require microtome sectioning (e.g., SBF-SEM) are not able to cut through certain materials, e.g., metals. As a result, mechanical removal of the metal from the bone-implant specimen, depending on the overall geometry and surface features, can unpredictably distort the integrity of the bone-implant interface zone. On the other hand, methods involving demineralisation (e.g., CLSM multiplexed imaging, bone CLARITY, SBF-SEM) pose the risk of distortion and displacement of metal implants and partial or complete elimination of acid-soluble CaP-based biomaterials. Although RCE does not require demineralisation or removal of a metal implant, minor technical difficulties may be experienced. For example, implant surfaces that are relatively smooth tend to afford poor mechanical interlocking between the implant and bone. Here, tissue distortion during sample preparation (i.e., shrinkage) allows for the development of a narrow gap at the bone-implant junction. This gap is subsequently filled by a thin layer of the embedding medium, which obscures the direct observation of osteocyte-implant contact using RCE [71, 72]. Canaliculi that had been in direct contact with the implant surface, while in situ, tend to appear separated from the implant surface. Certain experimental procedures also preclude direct visualisation of osteocyte attachment to the implant surface. Examples include various biomechanical tests to determine the strength of implant anchorage in bone, e.g., removal torque measurements [67], whereby the bone-implant interface is intentionally disrupted.

In Conclusion

Although RCE has also found usefulness in comparing the Ot.LCN with matrix bound cells such as cementocytes (in cementum) [134] and odontoblasts (in dentine) [135], this technique has been most valuable in providing novel insights into the Ot.LCN of bone. More recently, correlative use of RCE and multiple other techniques such as fluorochrome labelling, TEM, BSE-SEM, histology, immunohistochemistry, polarised light microscopy, and SBF-SEM, has led to the emergence of a new hypothesis that osteocytes may be capable of depositing bone mineral into the pericellular space [136]. While backscattered electron imaging of polished bone specimens is typically not permissive of visualising canalicular connectivity (e.g., at the bone-implant junction) or discontinuity (e.g., at cement lines), RCE facilitates correlative/site-specific assessment [137], which can be easily combined with quantitative backscattered electron imaging (qBEI) and energy dispersive X-ray spectroscopy (EDX)—all within the scanning electron microscope. Despite the minor shortcomings, RCE provides sophisticated, quantitative and qualitative information about the Ot.LCN. With the potential for universal application to resin embedded bone, RCE deserves to be exploited further. Novel biomaterial compositions, including those that undergo in vivo degradation or possess controlled release capabilities, are expected to be an important focus area where RCE can help address questions related to osseointegration and bone-bonding ability of biomaterials.

Acknowledgements This work was supported in part by the Japan Society for the Promotion of Science (JSPS; grant number 17K17564) and a grant from Takeda Science Foundation, the Svenska Sällskapet för Medicinsk Forskning (SSMF), the Hjalmar Svensson Foundation, and the Kungliga Vetenskaps-och Vitterhets-Samhället i Göteborg.

Author Contributions MS: Drafted and critically revised the work. FAS: Performed literature search and data analysis. Drafted and critically revised the work.

Funding Open access funding provided by University of Gothenburg. Japan Society for the Promotion of Science, Takeda Science Foundation, Svenska Sällskapet för Medicinsk Forskning, Stiftelsen Handlanden Hjalmar Svenssons, Kungl. Vetenskaps- och Vitterhets-Samhället i Göteborg

Declarations

Competing interests The authors have no relevant financial or non-financial interests to disclose.

References

1. Dallas SL, Prideaux M, Bonewald LF (2013) The osteocyte: an endocrine cell … and more. Endocr Rev 34:658–690
2. Kerschnitzki M, Kollmannsberger P, Burghammer M, Duda GN, Weinkamer R, Wagermaier W, Fratzl P (2013) Architecture of the osteocyte network correlates with bone material quality. J Bone Miner Res 28:1837–1845
3. van Tol AF, Schemenz V, Wagermaier W, Roschger A, Razi H, Vitienes I, Fratzl P, Willie BM, Weinkamer R (2020) The mechanoresponse of bone is closely related to the osteocyte lacunocanalicular network architecture. Proc Natl Acad Sci USA 117:32251–32259
4. Plotkin LI, Bellido T (2016) Osteocytic signalling pathways as therapeutic targets for bone fragility. Nat Rev Endocrinol 12:593–605
5. Qin L, Liu W, Cao H, Xiao G (2020) Molecular mechanosensors in osteocytes. Bone Res 8:23
6. Bonewald LF (2010) The osteocyte network as a source and reservoir of signaling factors. Endocrinol Metab 25:161–165
7. Bonewald LF, Wacker MJ (2013) FGF23 production by osteocytes. Pediatr Nephrol 28:563–568
8. Moharrer Y, Boerckel JD (2021) Tunnels in the rock: dynamics of osteocyte morphogenesis. Bone 153:116104
9. Qing H, Bonewald LF (2009) Osteocyte remodeling of the perilacunar and pericanalicular matrix. Int J Oral Sci 1:59–65
10. Buenzli PR, Sims NA (2015) Quantifying the osteocyte network in the human skeleton. Bone 75:144–150
11. Lara-Castillo N, Johnson ML (2020) Bone-muscle mutual interactions. Curr Osteoporos Rep 18:408–421
12. Lanske B, Densmore MJ, Erben RG (2014) Vitamin D endocrine system and osteocytes. Bonekey Rep 3:494
13. Weinkamer R, Kollmannsberger P, Fratzl P (2019) Towards a connectomic description of the osteocyte lacunocanalicular network in bone. Curr Osteoporos Rep 17:186–194
14. Manolagas SC (2010) From estrogen-centric to aging and oxidative stress: a revised perspective of the pathogenesis of osteoporosis. Endocr Rev 31:266–300
15. Shimizu T, Fujita N, Tsuji-Tamura K, Kitagawa Y, Fujisawa T, Tamura M, Sato M (2021) Osteocytes as main responders to low-intensity pulsed ultrasound treatment during fracture healing. Sci Rep 11:10298
16. Lai X, Price C, Modla S, Thompson WR, Caplan J, Kirn-Safran CB, Wang L (2015) The dependences of osteocyte network on bone compartment, age, and disease. Bone Res 3:15009
17. Shah FA, Thomsen P, Palmquist A (2018) A review of the impact of implant biomaterials on osteocytes. J Dent Res 97:977–986
18. Goggin PM, Zygalakis KC, Oreffo RO, Schneider P (2016) High-resolution 3D imaging of osteocytes and computational modelling in mechanobiology: insights on bone development, ageing, health and disease. Eur Cell Mater 31:264–295
19. Kubek DJ, Gattone VH, Allen MR (2010) Methodological assessment of acid-etching for visualizing the osteocyte lacunar-canalicular networks using scanning electron microscopy. Microsc Res Tech 73:182–186
20. Shah FA, Ruscsák K, Palmquist A (2019) 50 years of scanning electron microscopy of bone—a comprehensive overview of the important discoveries made and insights gained into bone material properties in health, disease, and taphonomy. Bone Res 7:15
21. Curtis TA, Ashrafi SH, Weber DF (1985) Canalicular communication in the cortices of human long bones. Anat Rec 212:336–344
22. Rubinacci A, Covini M, Bisogni C, Villa I, Galli M, Palumbo C, Ferretti M, Muglia MA, Marotti G (2002) Bone as an ion exchange system: evidence for a link between mechanotransduction and metabolic needs. Am J Physiol Endocrinol Metab 282:E851-864
23. Lampi T, Dekker H, Ten Bruggenkate CM, Schulten E, Mikkonen JJW, Koistinen A, Kullaa AM (2018) Acid-etching technique of non-decalcified bone samples for visualizing osteocyte-lacuno-canalicular network using scanning electron microscope. Ultrastruct Pathol 42:74–79
24. Shah FA, Johansson BR, Thomsen P, Palmquist A (2015) Ultrastructural evaluation of shrinkage artefacts induced by fixatives and embedding resins on osteocyte processes and pericellular space dimensions. J Biomed Mater Res A 103:1565–1576
25. Okada S, Yoshida S, Ashrafi SH, Schraufnagel DE (2002) The canalicular structure of compact bone in the rat at different ages. Microsc Microanal 8:104–115
26. Pazzaglia UE, Congiu T (2013) The cast imaging of the osteon lacunar-canalicular system and the implications with functional models of intracanalicular flow. J Anat 222:193–202
27. Qin W, Li X, Peng Y, Harlow LM, Ren Y, Wu Y, Li J, Qin Y, Sun J, Zheng S, Brown T, Feng JQ, Ke HZ, Bauman WA, Cardozo CC (2015) Sclerostin antibody preserves the morphology and structure of osteocytes and blocks the severe skeletal deterioration after motor-complete spinal cord injury in rats. J Bone Miner Res 30:1994–2004
28. Milovanovic P, Zimmermann EA, Hahn M, Djonic D, Püschel K, Djuric M, Amling M, Busse B (2013) Osteocytic canalicular networks: morphological implications for altered mechanosensitivity. ACS Nano 7:7542–7551
29. Rolvien T, Milovanovic P, Schmidt FN, von Kroge S, Wölfel EM, Krause M, Wulff B, Püschel K, Ritchie RO, Amling M, Busse B (2020) Long-term immobilization in elderly females causes a specific pattern of cortical bone and osteocyte deterioration different from postmenopausal osteoporosis. J Bone Miner Res 35:1343–1351
30. Karazisis D, Rasmusson L, Petronis S, Palmquist A, Shah FA, Agheli H, Emanuelsson L, Johansson A, Omar O, Thomsen P (2021) The effects of controlled nanotopography, machined topography and their combination on molecular activities, bone formation and biomechanical stability during osseointegration. Acta Biomater 136:279–290
31. Rolvien T, Nagel F, Milovanovic P, Wuertz S, Marshall RP, Jeschke A, Schmidt FN, Hahn M, Witten PE, Amling M, Busse B (2016) How the European eel (*Anguilla anguilla*) loses its skeletal framework across lifetime. Proc Biol Sci 283:20161550
32. Rolvien T, Schmidt FN, Milovanovic P, Jähn K, Riedel C, Butscheidt S, Püschel K, Jeschke A, Amling M, Busse B (2018) Early bone tissue aging in human auditory ossicles is accompanied by excessive hypermineralization, osteocyte death and micropetrosis. Sci Rep 8:1920
33. Zhang D, Miranda M, Li X, Han J, Sun Y, Rojas N, He S, Hu M, Lin L, Li X, Ke HZ, Qin YX (2019) Retention of osteocytic micromorphology by sclerostin antibody in a concurrent ovariectomy and functional disuse model. Ann N Y Acad Sci 1442:91–103
34. ten Dijke P, Krause C, de Gorter DJ, Löwik CW, van Bezooijen RL (2008) Osteocyte-derived sclerostin inhibits bone

formation: its role in bone morphogenetic protein and Wnt signaling. J Bone Joint Surg Am 90(Suppl 1):31–35
35. Stern AR, Yao X, Wang Y, Berhe A, Dallas M, Johnson ML, Yao W, Kimmel DB, Lane NE (2018) Effect of osteoporosis treatment agents on the cortical bone osteocyte microenvironment in adult estrogen-deficient, osteopenic rats. Bone Rep 8:115–124
36. Choy MV, Wong RM, Li MC, Wang BY, Liu XD, Lee W, Cheng JC, Chow SK, Cheung WH (2020) Can we enhance osteoporotic metaphyseal fracture healing through enhancing ultrastructural and functional changes of osteocytes in cortical bone with low-magnitude high-frequency vibration? FASEB J 34:4234–4252
37. Rolvien T, Amling M (2022) Disuse osteoporosis: clinical and mechanistic insights. Calcif Tissue Int 110:592–604
38. Shao X, Yan Z, Wang D, Yang Y, Ding Y, Luo E, Jing D, Cai J (2021) Pulsed electromagnetic fields ameliorate skeletal deterioration in bone mass, microarchitecture, and strength by enhancing canonical wnt signaling-mediated bone formation in rats with spinal cord injury. J Neurotrauma 38:765–776
39. Qing H, Ardeshirpour L, Pajevic PD, Dusevich V, Jähn K, Kato S, Wysolmerski J, Bonewald LF (2012) Demonstration of osteocytic perilacunar/canalicular remodeling in mice during lactation. J Bone Miner Res 27:1018–1029
40. Wysolmerski JJ (2012) Osteocytic osteolysis: time for a second look? Bonekey Rep 1:229
41. Prasadam I, Farnaghi S, Feng JQ, Gu W, Perry S, Crawford R, Xiao Y (2013) Impact of extracellular matrix derived from osteoarthritis subchondral bone osteoblasts on osteocytes: role of integrinβ1 and focal adhesion kinase signaling cues. Arthritis Res Ther 15:R150
42. Heinonen V, Ruotsalainen TJ, Paavola L, Mikkonen JJ, Asikainen P, Koistinen AP, Kullaa AM (2018) Alveolar bone remodeling after tooth extraction in irradiated mandible: an experimental study with canine model. Ultrastruct Pathol 42:124–132
43. Padala SR, Asikainen P, Ruotsalainen T, Mikkonen JJ, Silvast TS, Koistinen AP, Schulten E, Ten Bruggenkate CM, Kullaa AM (2021) Effects of irradiation in the mandibular bone loaded with dental implants. an experimental study with a canine model. Ultrastruct Pathol 45:276–285
44. Rios HF, Ye L, Dusevich V, Eick D, Bonewald LF, Feng JQ (2005) DMP1 is essential for osteocyte formation and function. J Musculoskelet Neuronal Interact 5:325–327
45. Feng JQ, Ward LM, Liu S, Lu Y, Xie Y, Yuan B, Yu X, Rauch F, Davis SI, Zhang S, Rios H, Drezner MK, Quarles LD, Bonewald LF, White KE (2006) Loss of DMP1 causes rickets and osteomalacia and identifies a role for osteocytes in mineral metabolism. Nat Genet 38:1310–1315
46. Lu Y, Yuan B, Qin C, Cao Z, Xie Y, Dallas SL, McKee MD, Drezner MK, Bonewald LF, Feng JQ (2011) The biological function of DMP-1 in osteocyte maturation is mediated by its 57-kDa C-terminal fragment. J Bone Miner Res 26:331–340
47. Ye L, Zhang S, Ke H, Bonewald LF, Feng JQ (2008) Periodontal breakdown in the Dmp1 null mouse model of hypophosphatemic rickets. J Dent Res 87:624–629
48. Gibson MP, Zhu Q, Wang S, Liu Q, Liu Y, Wang X, Yuan B, Ruest LB, Feng JQ, D'Souza RN, Qin C, Lu Y (2013) The rescue of dentin matrix protein 1 (DMP1)-deficient tooth defects by the transgenic expression of dentin sialophosphoprotein (DSPP) indicates that DSPP is a downstream effector molecule of DMP1 in dentinogenesis. J Biol Chem 288:7204–7214
49. Jani PH, Gibson MP, Liu C, Zhang H, Wang X, Lu Y, Qin C (2016) Transgenic expression of Dspp partially rescued the long bone defects of Dmp1-null mice. Matrix Biol 52–54:95–112
50. Rangiani A, Cao Z, Sun Y, Lu Y, Gao T, Yuan B, Rodgers A, Qin C, Kuro OM, Feng JQ (2012) Protective roles of DMP1 in high phosphate homeostasis. PLoS ONE 7:e42329
51. Gibson MP, Zhu Q, Liu Q, D'Souza RN, Feng JQ, Qin C (2013) Loss of dentin sialophosphoprotein leads to periodontal diseases in mice. J Periodontal Res 48:221–227
52. Gibson MP, Jani P, Wang X, Lu Y, Qin C (2014) Overexpressing the NH(2)-terminal fragment of dentin sialophosphoprotein (DSPP) aggravates the periodontal defects in Dspp knockout mice. J Oral Biosci 56:143–148
53. Dussold C, Gerber C, White S, Wang X, Qi L, Francis C, Capella M, Courbon G, Wang J, Li C, Feng JQ, Isakova T, Wolf M, David V, Martin A (2019) DMP1 prevents osteocyte alterations, FGF23 elevation and left ventricular hypertrophy in mice with chronic kidney disease. Bone Res 7:12
54. Zhou X, Zhang Z, Feng JQ, Dusevich VM, Sinha K, Zhang H, Darnay BG, de Crombrugghe B (2010) Multiple functions of osterix are required for bone growth and homeostasis in postnatal mice. Proc Natl Acad Sci USA 107:12919–12924
55. Kamiya N, Shuxian L, Yamaguchi R, Phipps M, Aruwajoye O, Adapala NS, Yuan H, Kim HK, Feng JQ (2016) Targeted disruption of BMP signaling through type IA receptor (BMPR1A) in osteocyte suppresses SOST and RANKL, leading to dramatic increase in bone mass, bone mineral density and mechanical strength. Bone 91:53–63
56. Kyono A, Avishai N, Ouyang Z, Landreth GE, Murakami S (2012) FGF and ERK signaling coordinately regulate mineralization-related genes and play essential roles in osteocyte differentiation. J Bone Miner Metab 30:19–30
57. Kühnisch J, Seto J, Lange C, Stumpp S, Kobus K, Grohmann J, Elefteriou F, Fratzl P, Mundlos S, Kolanczyk M (2014) Neurofibromin inactivation impairs osteocyte development in Nf1Prx1 and Nf1Col1 mouse models. Bone 66:155–162
58. Kamiya N, Yamaguchi R, Aruwajoye O, Kim AJ, Kuroyanagi G, Phipps M, Adapala NS, Feng JQ, Kim HK (2017) Targeted disruption of NF1 in osteocytes increases FGF23 and osteoid with osteomalacia-like bone phenotype. J Bone Miner Res 32:1716–1726
59. Wittrant Y, Gorin Y, Mohan S, Wagner B, Abboud-Werner SL (2009) Colony-stimulating factor-1 (CSF-1) directly inhibits receptor activator of nuclear factor-κB ligand (RANKL) expression by osteoblasts. Endocrinology 150:4977–4988
60. Harris SE, MacDougall M, Horn D, Woodruff K, Zimmer SN, Rebel VI, Fajardo R, Feng JQ, Gluhak-Heinrich J, Harris MA, Abboud Werner S (2012) Meox2Cre-mediated disruption of CSF-1 leads to osteopetrosis and osteocyte defects. Bone 50:42–53
61. Hao J, Narayanan K, Muni T, Ramachandran A, George A (2007) Dentin matrix protein 4, a novel secretory calcium-binding protein that modulates odontoblast differentiation. J Biol Chem 282:15357–15365
62. Huang Y, Chen H, Zhang H, Lu Y, Qin C (2021) FAM20C plays a critical role in the development of mouse vertebra. Spine J 22:337–348
63. Wang X, Wang S, Li C, Gao T, Liu Y, Rangiani A, Sun Y, Hao J, George A, Lu Y, Groppe J, Yuan B, Feng JQ, Qin C (2012) Inactivation of a novel FGF23 regulator, FAM20C, leads to hypophosphatemic rickets in mice. PLoS Genet 8:e1002708
64. Yuan B, Takaiwa M, Clemens TL, Feng JQ, Kumar R, Rowe PS, Xie Y, Drezner MK (2008) Aberrant Phex function in osteoblasts and osteocytes alone underlies murine X-linked hypophosphatemia. J Clin Invest 118:722–734
65. Zuo GL, Zhang LF, Qi J, Kang H, Jia P, Chen H, Shen X, Guo L, Zhou HB, Wang JS, Zhou Q, Qian ND, Deng LF (2015)

Activation of HIFa pathway in mature osteoblasts disrupts the integrity of the osteocyte/canalicular network. PLoS ONE 10:e0121266

66. Shah FA, Thomsen P, Palmquist A (2019) Osseointegration and current interpretations of the bone-implant interface. Acta Biomater 84:1–15
67. Shah FA, Johansson ML, Omar O, Simonsson H, Palmquist A, Thomsen P (2016) Laser-modified surface enhances osseointegration and biomechanical anchorage of commercially pure titanium implants for bone-anchored hearing systems. PLoS ONE 11:e0157504
68. Shah FA, Snis A, Matic A, Thomsen P, Palmquist A (2016) 3D printed Ti6Al4V implant surface promotes bone maturation and retains a higher density of less aged osteocytes at the bone-implant interface. Acta Biomater 30:357–367
69. Shah FA, Omar O, Suska F, Snis A, Matic A, Emanuelsson L, Norlindh B, Lausmaa J, Thomsen P, Palmquist A (2016) Long-term osseointegration of 3D printed CoCr constructs with an interconnected open-pore architecture prepared by electron beam melting. Acta Biomater 36:296–309
70. Shah FA, Jergéus E, Chiba A, Palmquist A (2018) Osseointegration of 3D printed microalloyed CoCr implants—Addition of 0.04% Zr to CoCr does not alter bone material properties. J Biomed Mater Res A 106:1655–1663
71. Shah FA, Stenlund P, Martinelli A, Thomsen P, Palmquist A (2016) Direct communication between osteocytes and acid-etched titanium implants with a sub-micron topography. J Mater Sci Mater Med 27:167
72. Du Z, Ivanovski S, Hamlet SM, Feng JQ, Xiao Y (2016) The Ultrastructural relationship between osteocytes and dental implants following osseointegration. Clin Implant Dent Relat Res 18:270–280
73. Du Z, Xiao Y, Hashimi S, Hamlet SM, Ivanovski S (2016) The effects of implant topography on osseointegration under estrogen deficiency induced osteoporotic conditions: histomorphometric, transcriptional and ultrastructural analysis. Acta Biomater 42:351–363
74. He X, Yamada M, Watanabe J, Tiskratok W, Ishibashi M, Kitaura H, Mizoguchi I, Egusa H (2022) Titanium nanotopography induces osteocyte lacunar-canalicular networks to strengthen osseointegration. Acta Biomater 151:613–627
75. Shah FA, Wang X, Thomsen P, Grandfield K, Palmquist A (2015) High-resolution visualization of the osteocyte lacuno-canalicular network juxtaposed to the surface of nanotextured titanium implants in human. ACS Biomater Sci Eng 1:305–313
76. Liu B, Ma Z, Li J, Xie H, Wei X, Wang B, Tian S, Yang J, Yang L, Cheng L, Li L, Zhao D (2022) Experimental study of a 3D printed permanent implantable porous Ta-coated bone plate for fracture fixation. Bioact Mater 10:269–280
77. Sasaki M, Kuroshima S, Aoki Y, Inaba N, Sawase T (2015) Ultrastructural alterations of osteocyte morphology via loaded implants in rabbit tibiae. J Biomech 48:4130–4141
78. Gorustovich AA (2010) Imaging resin-cast osteocyte lacuno-canalicular system at bone-bioactive glass interface by scanning electron microscopy. Microsc Microanal 16:132–136
79. Shah FA, Jolic M, Micheletti C, Omar O, Norlindh B, Emanuelsson L, Engqvist H, Engstrand T, Palmquist A, Thomsen P (2023) Bone without borders—monetite-based calcium phosphate guides bone formation beyond the skeletal envelope. Bioact Mater 19:103–114
80. Fricain JC, Aid R, Lanouar S, Maurel DB, Le Nihouannen D, Delmond S, Letourneur D, Amedee Vilamitjana J, Catros S (2018) In-vitro and in-vivo design and validation of an injectable polysaccharide-hydroxyapatite composite material for sinus floor augmentation. Dent Mater 34:1024–1035
81. Quent VM, Theodoropoulos C, Hutmacher DW, Reichert JC (2016) Differential osteogenicity of multiple donor-derived human mesenchymal stem cells and osteoblasts in monolayer, scaffold-based 3D culture and in vivo. Biomed Tech (Berl) 61:253–266
82. Henkel J, Medeiros Savi F, Berner A, Fountain S, Saifzadeh S, Steck R, Epari DR, Woodruff MA, Knackstedt M, Schuetz MA, Hutmacher DW (2021) Scaffold-guided bone regeneration in large volume tibial segmental defects. Bone 153:116163
83. Holzapfel BM, Wagner F, Loessner D, Holzapfel NP, Thibaudeau L, Crawford R, Ling MT, Clements JA, Russell PJ, Hutmacher DW (2014) Species-specific homing mechanisms of human prostate cancer metastasis in tissue engineered bone. Biomaterials 35:4108–4115
84. Holzapfel BM, Hutmacher DW, Nowlan B, Barbier V, Thibaudeau L, Theodoropoulos C, Hooper JD, Loessner D, Clements JA, Russell PJ, Pettit AR, Winkler IG, Levesque JP (2015) Tissue engineered humanized bone supports human hematopoiesis in vivo. Biomaterials 61:103–114
85. Brierly GI, Ren J, Baldwin J, Saifzadeh S, Theodoropoulos C, Tsurkan MV, Lynham A, Hsu E, Nikolarakos D, Werner C, Woodruff MA, Hutmacher DW, Bray LJ (2019) Investigation of sustained BMP delivery in the prevention of medication-related osteonecrosis of the jaw (MRONJ) in a rat model. Macromol Biosci 19:e1900226
86. Liu W, Zhang D, Li X, Zheng L, Cui C, Cui Y, Sun J, Xie J, Zhou X (2019) TGF-β1 facilitates cell-cell communication in osteocytes via connexin43- and pannexin1-dependent gap junctions. Cell Death Discov 5:141
87. Shokoohmand A, Ren J, Baldwin J, Atack A, Shafiee A, Theodoropoulos C, Wille ML, Tran PA, Bray LJ, Smith D, Chetty N, Pollock PM, Hutmacher DW, Clements JA, Williams ED, Bock N (2019) Microenvironment engineering of osteoblastic bone metastases reveals osteomimicry of patient-derived prostate cancer xenografts. Biomaterials 220:119402
88. Jeon JE, Vaquette C, Theodoropoulos C, Klein TJ, Hutmacher DW (2014) Multiphasic construct studied in an ectopic osteochondral defect model. J R Soc Interface 11:20140184
89. Shah FA, Palmquist A (2017) Evidence that osteocytes in autogenous bone fragments can repair disrupted canalicular networks and connect with osteocytes in de novo formed bone on the fragment surface. Calcif Tissue Int 101:321–327
90. Rolvien T, Hahn M, Siebert U, Püschel K, Wilke HJ, Busse B, Amling M, Oheim R (2017) Vertebral bone microarchitecture and osteocyte characteristics of three toothed whale species with varying diving behaviour. Sci Rep 7:1604
91. Lindgren J, Uvdal P, Engdahl A, Lee AH, Alwmark C, Bergquist KE, Nilsson E, Ekström P, Rasmussen M, Douglas DA, Polcyn MJ, Jacobs LL (2011) Microspectroscopic evidence of cretaceous bone proteins. PLoS ONE 6:e19445
92. Micheletti C, DiCecco L-A, Larsson Wexell C, Binkley DM, Palmquist A, Grandfield K, Shah FA (2022) Multimodal and multiscale characterization of the bone-bacteria interface in a case of medication-related osteonecrosis of the jaw. JBMR Plus 6:e10693
93. Wang L, Shao J, Ye T, Deng L, Qiu S (2012) Three-dimensional morphology of microdamage in peri-screw bone: a scanning electron microscopy of methylmethacrylate cast replica. Microsc Microanal 18:1106–1111
94. Ngo L, Nathanson AD, Garbowski T, Knothe U, Zeidler D, Knothe Tate ML (2019) Electron microscopy sample preparation protocol enabling nano-to-mesoscopic mapping of cellular connectomes and their habitats in human tissues and organs. Bio Protoc 9:e3298
95. Knothe Tate ML, Zeidler D, Pereira AF, Hageman D, Garbowski T, Mishra S, Gardner L, Knothe UR (2016) Organ-to-cell-scale

health assessment using geographical information system approaches with multibeam scanning electron microscopy. Adv Healthc Mater 5:1581–1587

96. Knothe Tate ML, Srikantha A, Wojek C, Zeidler D (2021) Connectomics of bone to brain-probing physical renderings of cellular experience. Front Physiol 12:647603
97. Palmquist A (2018) A multiscale analytical approach to evaluate osseointegration. J Mater Sci Mater Med 29:60
98. Ejiri S, Ozawa H (1982) Scanning electron microscopic observations of rat tibia using the HCl-collagenase method. Arch Histol Jpn 45:399–404
99. Abe K, Hashizume H, Ushiki T (1992) An EDTA-KOH method to expose bone cells for scanning electron microscopy. J Electron Microsc (Tokyo) 41:113–115
100. Yamamoto T, Hasegawa T, Sasaki M, Hongo H, Tabata C, Liu Z, Li M, Amizuka N (2012) Structure and formation of the twisted plywood pattern of collagen fibrils in rat lamellar bone. J Electron Microsc (Tokyo) 61:113–121
101. Schneider P, Meier M, Wepf R, Muller R (2011) Serial FIB/SEM imaging for quantitative 3D assessment of the osteocyte lacuno-canalicular network. Bone 49:304–311
102. Tabata K, Hashimoto M, Takahashi H, Wang Z, Nagaoka N, Hara T, Kamioka H (2022) A morphometric analysis of the osteocyte canaliculus using applied automatic semantic segmentation by machine learning. J Bone Miner Metab 40:571–580
103. Binkley DM, Deering J, Yuan H, Gourrier A, Grandfield K (2020) Ellipsoidal mesoscale mineralization pattern in human cortical bone revealed in 3D by plasma focused ion beam serial sectioning. J Struct Biol 212:107615
104. Goggin P, Ho EML, Gnaegi H, Searle S, Oreffo ROC, Schneider P (2020) Development of protocols for the first serial block-face scanning electron microscopy (SBF SEM) studies of bone tissue. Bone 131:115107
105. You LD, Weinbaum S, Cowin SC, Schaffler MB (2004) Ultrastructure of the osteocyte process and its pericellular matrix. Anat Rec A Discov Mol Cell Evol Biol 278:505–513
106. Sennerby L, Thomsen P, Ericson LE (1993) Early tissue response to titanium implants inserted in rabbit cortical bone. J Mater Sci Mater Med 4:494–502
107. Thomsen P, Larsson C, Ericson LE, Sennerby L, Lausmaa J, Kasemo B (1997) Structure of the interface between rabbit cortical bone and implants of gold, zirconium and titanium. J Mater Sci Mater Med 8:653–665
108. Steflik DE, Hanes PJ, Sisk AL, Parr GR, Song MJ, Lake FT, McKinney RV (1992) Transmission electron microscopic and high voltage electron microscopic observations of the bone and osteocyte activity adjacent to unloaded dental implants placed in dogs. J Periodontol 63:443–452
109. Steflik DE, Sisk AL, Parr GR, Lake FT, Hanes PJ, Berkery DJ, Brewer P (1994) Transmission electron and high-voltage electron microscopy of osteocyte cellular processes extending to the dental implant surface. J Biomed Mater Res 28:1095–1107
110. Steflik DE, Corpe RS, Lake FT, Young TR, Sisk AL, Parr GR, Hanes PJ, Berkery DJ (1998) Ultrastructural analyses of the attachment (bonding) zone between bone and implanted biomaterials. J Biomed Mater Res 39:611–620
111. Shah FA, Nilson B, Brånemark R, Thomsen P, Palmquist A (2014) The bone-implant interface—nanoscale analysis of clinically retrieved dental implants. Nanomedicine 10:1729–1737
112. Shah FA, Lee BEJ, Tedesco J, Larsson Wexell C, Persson C, Thomsen P, Grandfield K, Palmquist A (2017) Micrometer-sized magnesium whitlockite crystals in micropetrosis of bisphosphonate-exposed human alveolar bone. Nano Lett 17:6210–6216
113. Kamioka H, Kameo Y, Imai Y, Bakker AD, Bacabac RG, Yamada N, Takaoka A, Yamashiro T, Adachi T, Klein-Nulend J (2012) Microscale fluid flow analysis in a human osteocyte canaliculus using a realistic high-resolution image-based three-dimensional model. Integr Biol (Camb) 4:1198–1206
114. Kamioka H, Murshid SA, Ishihara Y, Kajimura N, Hasegawa T, Ando R, Sugawara Y, Yamashiro T, Takaoka A, Takano-Yamamoto T (2009) A method for observing silver-stained osteocytes <i>In Situ</i> in 3-μm sections using ultra-high voltage electron microscopy tomography. Microsc Microanal 15:377–383
115. Genthial R, Beaurepaire E, Schanne-Klein MC, Peyrin F, Farlay D, Olivier C, Bala Y, Boivin G, Vial JC, Debarre D, Gourrier A (2017) Label-free imaging of bone multiscale porosity and interfaces using third-harmonic generation microscopy. Sci Rep 7:3419
116. Ren Y, Lin S, Jing Y, Dechow PC, Feng JQ (2014) A novel way to statistically analyze morphologic changes in Dmp1-null osteocytes. Connect Tissue Res 55(Suppl 1):129–133
117. Repp F, Kollmannsberger P, Roschger A, Kerschnitzki M, Berzlanovich A, Gruber GM, Roschger P, Wagermaier W, Weinkamer R (2017) Spatial heterogeneity in the canalicular density of the osteocyte network in human osteons. Bone Rep 6:101–108
118. Kamioka H, Honjo T, Takano-Yamamoto T (2001) A three-dimensional distribution of osteocyte processes revealed by the combination of confocal laser scanning microscopy and differential interference contrast microscopy. Bone 28:145–149
119. Ishihara Y, Kamioka H, Honjo T, Ueda H, Takano-Yamamoto T, Yamashiro T (2008) Hormonal, pH, and calcium regulation of connexin 43-mediated dye transfer in osteocytes in chick calvaria. J Bone Miner Res 23:350–360
120. Sugawara Y, Ando R, Kamioka H, Ishihara Y, Honjo T, Kawanabe N, Kurosaka H, Takano-Yamamoto T, Yamashiro T (2011) The three-dimensional morphometry and cell-cell communication of the osteocyte network in chick and mouse embryonic calvaria. Calcif Tissue Int 88:416–424
121. Kamioka H, Ishihara Y, Ris H, Murshid SA, Sugawara Y, Takano-Yamamoto T, Lim SS (2007) Primary cultures of chick osteocytes retain functional gap junctions between osteocytes and between osteocytes and osteoblasts. Microsc Microanal 13:108–117
122. Kamel-ElSayed SA, Tiede-Lewis LM, Lu Y, Veno PA, Dallas SL (2015) Novel approaches for two and three dimensional multiplexed imaging of osteocytes. Bone 76:129–140
123. Kim J, Bixel MG (2020) Intravital multiphoton imaging of the bone and bone marrow environment. Cytometry A 97:496–503
124. Sano H, Kikuta J, Furuya M, Kondo N, Endo N, Ishii M (2015) Intravital bone imaging by two-photon excitation microscopy to identify osteocytic osteolysis in vivo. Bone 74:134–139
125. Tokarz D, Cisek R, Wein MN, Turcotte R, Haase C, Yeh SA, Bharadwaj S, Raphael AP, Paudel H, Alt C, Liu TM, Kronenberg HM, Lin CP (2017) Intravital imaging of osteocytes in mouse calvaria using third harmonic generation microscopy. PLoS ONE 12:e0186846
126. Casanova M, Schindeler A, Peacock L, Lee L, Schneider P, Little DG, Müller R (2021) Characterization of the developing lacuno-canalicular network during fracture repair. JBMR Plus 5:e10525
127. Greenbaum A, Chan KY, Dobreva T, Brown D, Balani DH, Boyce R, Kronenberg HM, McBride HJ, Gradinaru V (2017) Bone CLARITY: Clearing, imaging, and computational analysis of osteoprogenitors within intact bone marrow. Sci Transl Med 9:eaah6518
128. Dierolf M, Menzel A, Thibault P, Schneider P, Kewish CM, Wepf R, Bunk O, Pfeiffer F (2010) Ptychographic X-ray computed tomography at the nanoscale. Nature 467:436–439
129. Dong P, Haupert S, Hesse B, Langer M, Gouttenoire P-J, Bousson V, Peyrin F (2014) 3D osteocyte lacunar morphometric properties and distributions in human femoral cortical bone using synchrotron radiation micro-CT images. Bone 60:172–185

130. Langer M, Pacureanu A, Suhonen H, Grimal Q, Cloetens P, Peyrin F (2012) X-ray phase nanotomography resolves the 3D human bone ultrastructure. PLoS ONE 7:e35691
131. Bortel E, Grover LM, Eisenstein N, Seim C, Suhonen H, Pacureanu A, Westenberger P, Raum K, Langer M, Peyrin F, Addison O, Hesse B (2022) Interconnectivity explains high canalicular network robustness between neighboring osteocyte lacunae in human bone. Adv Nanobiomed Res 2:2100090
132. Katsamenis OL, Chong HMH, Andriotis OG, Thurner PJ (2013) Load-bearing in cortical bone microstructure: selective stiffening and heterogeneous strain distribution at the lamellar level. J Mech Behav Biomed Mater 17:152–165
133. Reilly GC, Knapp HF, Stemmer A, Niederer P, Knothe Tate ML (2001) Investigation of the morphology of the lacunocanalicular system of cortical bone using atomic force microscopy. Ann Biomed Eng 29:1074–1081
134. Zhao N, Nociti FH Jr, Duan P, Prideaux M, Zhao H, Foster BL, Somerman MJ, Bonewald LF (2016) Isolation and functional analysis of an immortalized murine cementocyte cell line, IDG-CM6. J Bone Miner Res 31:430–442
135. Lu Y, Xie Y, Zhang S, Dusevich V, Bonewald LF, Feng JQ (2007) DMP1-targeted Cre expression in odontoblasts and osteocytes. J Dent Res 86:320–325
136. Wang K, Ren Y, Lin S, Jing Y, Ma C, Wang J, Yuan XB, Han X, Zhao H, Wang Z, Zheng M, Xiao Y, Chen L, Olsen BR, Feng JQ (2021) Osteocytes but not osteoblasts directly build mineralized bone structures. Int J Biol Sci 17:2430–2448
137. Shah FA (2017) Osteocytes as indicators of bone quality - multiscale structure-composition characterisation of the bone-implant interface (PhD Thesis). Göteborgs Universitet, Göteborg